

On the Approximation of Transport Phenomena – a Dynamical Systems Approach

Michael Dellnitz^{*1}, Gary Froyland², Christian Horenkamp¹, and Kathrin Padberg^{3,4}

¹ Department of Mathematics, University of Paderborn, 33095 Paderborn, Germany

² School of Mathematics and Statistics, The University of New South Wales, Sydney NSW 2052, Australia

³ Institute for Transport and Economics, Dresden University of Technology, 01062 Dresden, Germany

⁴ Center for Information Services and High Performance Computing (ZIH), Dresden University of Technology, 01062 Dresden, Germany

Received 25 March 2009

Published online 19 May 2009

Key words Transfer operator, coherent structures, almost-invariant sets, ocean dynamics, three-body problem, transport rates.

MSC (2000) 37M25, 37N05, 37N10, 37N30

Transport phenomena are studied in a large variety of dynamical systems with applications ranging from the analysis of fluid flow in the ocean and the predator-prey interaction in jellyfish to the investigation of blood flow in the cardiovascular system. Our approach to analyze transport is based on the methodology of so-called *transfer operators* associated with a dynamical system since this is particularly suitable. We describe the approach and illustrate it by two real world applications: the computation of transport for asteroids in the solar system and the approximation of macroscopic structures in the Southern Ocean.

© 2009 WILEY-VCH Verlag GmbH & Co. KGaA, Weinheim

1 Introduction

Over the last years *set oriented* numerical methods have been developed in the context of the numerical treatment of dynamical systems. The basic idea is to capture the objects of interest – for instance *invariant manifolds* or *invariant measures* – by outer approximations which are created via adaptive multilevel subdivision techniques. These schemes work very much in the spirit of *cell mapping techniques* (see [15, 21]) but in addition they allow for an extremely memory and time efficient discretization of the phase space. Moreover they have the flexibility to be applied to several problem types, and in this contribution we will show that they are particularly useful in the analysis of *transport processes* in real world applications.

Today *transport* is a widely studied phenomenon in dynamical systems [13, 14, 16, 25, 30]. The applications range from the analysis of fluid flow in the ocean [10, 11] and the

* Corresponding author: e-mail: dellnitz@math.uni-paderborn.de, Phone: +49 5251 60 2649, Fax: +49 5251 60 4216

consideration of predator-prey interaction in jellyfish [24] to the investigation of blood flow in the cardiovascular system [26].

There are essentially two different mathematical concepts for studying transport. First there is a geometric approach where the transport phenomena are captured by *Lagrangian coherent structures* (LCS). In this case transport barriers are identified via the approximation of time-dependent invariant manifolds, for instance using *finite-time Lyapunov exponents* (FTLEs) [13, 14, 22, 25]. The second approach is based on the analysis of properties of *transfer operators*. This method is more measure theoretic in nature and it is therefore suitable for the application of set oriented numerical techniques. In this contribution it is our purpose to provide an insight into the set oriented approximation of transport phenomena; we base our exposition mainly on the publications [5, 6, 10, 11].

A more detailed outline of this article is as follows. In Section 2 we define the basic notions concerning the background on transfer operators, and in Section 3 we show how to approximate transfer operators and transport rates numerically in our set oriented framework. In Sections 4 and 5 we present examples from two real world applications, namely the computation of transport for asteroids in the solar system and the approximation of macroscopic (almost-invariant) structures in the Southern Ocean. While persistent ocean features such as gyres and eddies may be observed and tracked by satellite altimetry [12], detecting and tracking the regions that act as barriers to flow pathways is more ambiguous. These almost-invariant structures have a significant ecological impact including the trapping of material such as nutrients, phytoplankton and pollutants.

2 Preliminaries

We are interested in studying transport phenomena of a dynamical process described by an ordinary differential equation of the form

$$\dot{x} = f(t, x), \quad (1)$$

where $x \in X \subset \mathbb{R}^\ell$ and $f : \mathbb{R} \times X \rightarrow \mathbb{R}^\ell$ is smooth. We assume that the temporal evolution of the system takes place inside the state space X and that the solution operator $\phi : X \times \mathbb{R} \times \mathbb{R} \rightarrow X$ is well defined, i.e. $\phi(x_0, t_0; \cdot)$ is the solution of (1) starting at the initial state x_0 at time t_0 on \mathbb{R} . A set $A \subset X$ is ϕ -invariant over $[t, t + \tau]$ if $A = \phi(A, t + s; -s)$ for all $0 \leq s \leq \tau$.

Coherent structures obey an approximate invariance principle over short periods of time. We call a set $A \subset X$ *almost-invariant* with respect to a probability measure μ on X if $\mu(A) \neq 0$ and

$$\rho_{t,\tau}(A) = \frac{\mu(A \cap \phi(A, t + \tau; -\tau))}{\mu(A)} \approx 1. \quad (2)$$

The meaning of “ ≈ 1 ” has to be made precise in the actual application. The ratio in (2) is the proportion of the set A that remains in A after flowing from time t to time $t + \tau$, with respect to the measure μ . Clearly, the closer this ratio is to unity, the closer the set A is to being invariant. In order to discover coherent structures in the dynamics, we seek to find dominant almost-invariant sets.

An important quantity indicating the magnitude of transport w.r.t. μ between sets $A_1, A_2 \subset X$ over the time τ is given by

$$T_{A_1, A_2, t}(\tau) = \mu(A_1 \cap \phi(A_2, t + \tau; -\tau)). \quad (3)$$

In fact, $T_{A_1, A_2, t}(\tau)$ provides the *transport rate* by determining the measure of the subset of points flowing from A_1 to A_2 in time τ starting at time t .

Our approach is to use a transfer operator $\mathcal{P}_{t, \tau} : \mathcal{M} \rightarrow \mathcal{M}$ on the space of bounded complex valued measures to encode these transport quantities of the underlying dynamical system (see [4, 5, 6, 10, 11]). The transfer operator is defined by

$$(\mathcal{P}_{t, \tau} \nu)(A) = \nu(\phi(A, t + \tau; -\tau)), \quad A \subset X \text{ measurable}, \quad \nu \in \mathcal{M}. \quad (4)$$

This operator describes the evolution of bounded complex valued measures induced by the underlying dynamical system, i.e. if ν describes the distribution of particles at time t , then $\mathcal{P}_{t, \tau} \nu$ describes their distribution at time $t + \tau$.

3 Numerical Approximation

We now describe how to approximate the different quantities numerically. We begin with the transfer operator itself. Then we describe how to approximate transport rates directly, since we are going to use this technique in the computation of transport for asteroids in the solar system. Finally we indicate how to approximate almost-invariant sets and how to use them for the identification of transport phenomena.

3.1 Approximation of the Transfer Operator

In order to be able to analyze the properties of the infinite-dimensional transfer operator $\mathcal{P}_{t, \tau}$ we need an approximation of $\mathcal{P}_{t, \tau}$ by a finite dimensional linear operator. Let $\mathcal{B} = \{B_1, \dots, B_n\}$ denote a partition of X into connected compact boxes. Following Ulam [29], an approximation of the transfer operator $\mathcal{P}_{t, \tau}$ is given by the stochastic matrix

$$\mathbf{P}_{t, \tau; i, j} = \frac{m(B_j \cap \phi(B_i, t + \tau; -\tau))}{m(B_j)}, \quad (5)$$

where m represents normalized Lebesgue measure. The entry $\mathbf{P}_{t, \tau; i, j}$ may be interpreted as the probability that a point selected uniformly at random in B_j at time t will be in B_i at time $t + \tau$. Note that $\mathbf{P}_{t, \tau}$ is typically sparse and that $\mathbf{P}_{t, \tau}^T$ defines a finite Markov chain.

In numerical applications we proceed as follows: First we choose N uniformly distributed test points $y_{j, l} \in B_j$, $l = 1, \dots, N$, for each box B_j . Then, for each $j = 1, \dots, n$, we calculate $\phi(y_{j, l}, t; \tau)$, $l = 1, \dots, N$, via numerical integration and approximate $\mathbf{P}_{t, \tau; i, j}$ by

$$\mathbf{P}_{t, \tau; i, j} \approx \frac{\#\{l : y_{j, l} \in B_j, \phi(y_{j, l}, t; \tau) \in B_i\}}{N}. \quad (6)$$

Such a box-discretization of X and the construction of $\mathbf{P}_{t, \tau}$ is carried out efficiently using the software package GAIO [3]. From now on we will assume that the state space X is covered by a box-collection \mathcal{B} .

3.2 Transport Rates

For an approximation of the transport rates w.r.t. Lebesgue measure m – this is the situation we will be interested in in our first application – between two sets A_1 and A_2 (see (3)) we define $m_{A_1}(A_2) = m(A_1 \cap A_2)$ and observe that

$$\begin{aligned} (\mathcal{P}_{t,\tau} m_{A_1})(A_2) &= m_{A_1}(\phi(A_2, t + \tau; -\tau)) \\ &= m(A_1 \cap \phi(A_2, t + \tau; -\tau)) \\ &= T_{A_1, A_2, t}(\tau). \end{aligned}$$

In our application in Section 4 the underlying dynamical system is autonomous and we will consider a suitable Poincaré map for the transport calculations. In this case we denote by \mathcal{P} the corresponding transfer operator and by $T_{A_1, A_2}(k)$ the transport rate for k iterates of this map. Then we can compute transport rates as follows: For a subset $C \subset X$ we define the vectors $e_C, u_C \in \mathbb{R}^n$ – recall that the cardinality of \mathcal{B} is n – by

$$(e_C)_j = \begin{cases} 1, & \text{if } B_j \subset C, \\ 0, & \text{otherwise} \end{cases}, \quad (u_C)_j = \begin{cases} m(B_j), & \text{if } B_j \subset C, \\ 0, & \text{otherwise} \end{cases}. \quad (7)$$

Denote by \mathbf{P} the discretization of the transfer operator \mathcal{P} . Then the transport between the sets A_1 and A_2 , which are assumed to be the unions of boxes of \mathcal{B} , can be approximated via

$$T_{A_1, A_2}(k) \approx e_{A_2}^T \mathbf{P}^k u_{A_1}. \quad (8)$$

For a sequence $(\mathcal{B}_r)_r$ of partitions such that

$$\max_{B \in \mathcal{B}_r} \text{diam}(B) \rightarrow 0 \quad \text{as } r \rightarrow \infty, \quad (9)$$

where $r \in \mathbb{N}$, we can make this statement more precise with the following theorem:

Theorem 3.1 ([5]) *If $A_i \subset X, i = 1, 2$ are chosen such that for $i = 1, 2$*

$$m \left(\bigcup_{\substack{B \in \mathcal{B}_r \\ B \cap \partial A_i \neq \emptyset}} B \right) \rightarrow 0 \quad \text{as } r \rightarrow \infty, \quad (10)$$

then for every fixed k ,

$$e_{A_2}^T \mathbf{P}_{\mathcal{B}_r}^k u_{A_1} \rightarrow T_{A_1, A_2}(k) \quad \text{as } r \rightarrow \infty. \quad (11)$$

Here, $\mathbf{P}_{\mathcal{B}_r}$ denotes the approximation of the transfer operator with respect to the partition \mathcal{B}_r . For more details on this construction see [5, 6].

3.3 Almost-Invariant Sets

In this section, we relate the almost-invariance property (2) to real eigenvalues $\lambda \neq 1$ of $\mathcal{P}_{t,\tau}$ and corresponding real valued (signed) eigenmeasures ν , that is,

$$\mathcal{P}_{t,\tau} \nu = \lambda \nu. \quad (12)$$

We temporarily fix both the initial time t and the time of integration τ . It is well known that spectral properties of the transfer operator can be related to almost-invariance in the underlying dynamics. For instance, in [4] the following result has been shown in the situation where the underlying dynamical process is perturbed by small random perturbations:

Theorem 3.2 *Suppose that the eigenmeasure ν of $\mathcal{P}_{t,\tau}$ corresponding to the eigenvalue $\lambda \neq 1$ is scaled so that $|\nu|$ is a probability measure, and let $A \subset X$ be a set with $\nu(A) = \frac{1}{2}$. Then*

$$\rho_{t,\tau}(A) + \rho_{t,\tau}(X \setminus A) = \lambda + 1, \tag{13}$$

where $\rho_{t,\tau}$ is measured with respect to $|\nu|$.

Remark 3.3

- (a) Observe that (13) implies that both A and $X \setminus A$ are almost-invariant w.r.t. $|\nu|$ if the eigenvalue λ is close to one.
- (b) The eigenmeasure ν satisfies $\nu(X) = 0$. This follows from

$$\nu(X) = \nu(\phi(X, t + \tau; -\tau)) = (\mathcal{P}_{t,\tau}\nu)(X) = \lambda\nu(X)$$

since $\lambda \neq 1$. Combining $|\nu|(X) = 1$ and $\nu(X) = 0$, we can guarantee the existence of a set $A \subset X$ with $\nu(A) = \frac{1}{2}$.

Now we show how to compute $\rho_{t,\tau}(A)$ numerically. For this we assume the existence of a “natural” invariant measure μ (cf. [4]). Let $\mathcal{B} = \{B_1, \dots, B_n\}$ be a partition as defined previously. For $A \subset X$ we define

$$\mu_n(A) = \sum_{i=1}^n \frac{m(A \cap B_i)}{m(B_i)} p_i, \tag{14}$$

where $p \in \mathbb{R}^n$ is the normalized fixed left eigenvector of $\mathbf{P}_{t,\tau}^T$. So the invariant density p of the induced Markov chain is used to provide an approximation of the natural invariant measure μ . From now on let A be a union of boxes, i. e. $A = \cup_{i \in \mathcal{I}} B_i$ where $\mathcal{I} \subset \{1, \dots, n\}$. Then it is straightforward to show [8] that

$$\rho_{t,\tau}(A) = \frac{\sum_{i,j \in \mathcal{I}} p_i \mathbf{P}_{t,\tau}^{ji}}{\sum_{i \in \mathcal{I}} p_i}, \tag{15}$$

where $\rho_{t,\tau}$ is measured with respect to μ_n . For convergence results we refer to [8].

Transforming the matrix $\mathbf{P}_{t,\tau}$ into a “time symmetric” matrix $R_{t,\tau}$ yields

$$R_{t,\tau;i,j} = \left(\mathbf{P}_{t,\tau;j,i} + \frac{p_j \mathbf{P}_{t,\tau;i,j}}{p_i} \right) / 2. \tag{16}$$

The matrix $R_{t,\tau}$ is stochastic, has only real eigenvalues (see [2]) and satisfies important maximization properties related to almost-invariance. For instance, denote by λ_2 the second largest eigenvalue of $R_{t,\tau}$. Then, for $A \subset X$ as above, Froyland showed in [7] that

$$1 - \sqrt{2(1 - \lambda_2)} \leq \max_{0 \leq \mu_n(A) \leq 1/2} \rho_{t,\tau}(A) \leq \frac{1 + \lambda_2}{2}. \tag{17}$$

Observe that the matrix $R_{t,\tau;i,j}$ is typically sparse and the focus lies only on the large spectral values near to 1, which may be efficiently computed by Lanczos iteration methods.

4 Transport of Asteroids in the Solar System

In this first application (see [6]) we study the transport rates (3) for the movement of asteroids in the solar system. We are particularly interested in transitions between the so-called *quasi-Hilda region* and a region beyond the *Mars-crosser line*. For details on the astronomical background we refer to [27, 28] and for more applications of studying transport phenomena in the solar system we refer to [18, 19, 20].

4.1 The Dynamical System

For our computations we use as the dynamical model the *planar circular restricted three-body problem* (PCRTBP) with Sun and Jupiter as the primaries. Let us briefly summarize the main properties of this dynamical system (for a more detailed description we refer to [17, 28]): The Hamiltonian for the motion of a particle in the field of the Sun and Jupiter is given by

$$H = E = \frac{1}{2}(p_x^2 + p_y^2) - (xp_y - yp_x) - \frac{m_S}{r_S} - \frac{m_J}{r_J} - \frac{1}{2}m_S m_J, \quad (18)$$

where E is the energy, r_S and r_J are the distances between the particle and Sun and Jupiter, respectively. The quantities m_S and m_J are the (normalized) masses of Sun and Jupiter. In the PCRTBP the coordinate system rotates about the common center of mass. In this rotating frame (x, y) is the position of the particle relative to the positions of Sun and Jupiter, and $p_x = \dot{x} - y$, $p_y = \dot{y} + x$ are the conjugate momenta. Thus, the motion of the particle takes place on a three-dimensional energy manifold embedded in the four-dimensional phase space with coordinates (x, y, \dot{x}, \dot{y}) .

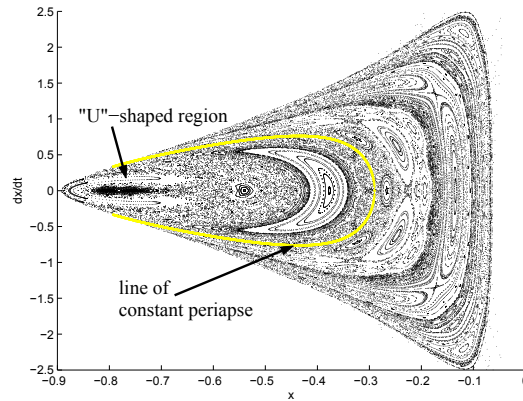


Fig. 1 (online colour at: www.gamm-mitteilungen.org) The mixed phase space structure of the PCRTBP is shown on the Poincaré section. The bright line corresponds to a line of constant periaipse. In this case the periaipse is equal to the semi-major axis of Mars' orbit around the Sun.

We choose a Poincaré section by $y = 0$ and $\dot{y} < 0$. The coordinates on the section are (x, \dot{x}) . As a further restriction, only the motion of particles in the interior to the orbit of the planet Jupiter are considered. For these orbits the Poincaré section is crossed every time the

test particle is aligned with Sun and Jupiter, along $x < 0$. That is, our section becomes the two-dimensional manifold M defined by $y = 0, \dot{y} < 0, x < 0$, reducing the system to an area and orientation preserving map $f : M \rightarrow M$ on a subset M of \mathbb{R}^2 . In Figure 1 we show a mixed phase space structure on this Poincaré section.

4.2 Numerical Results

The energy considered in this paper, $E = -1.52$, is just below that of the equilibrium point (Lagrange point) L_1 in the PCRTBP, and is a good starting point for understanding the dynamics related to the Hilda resonance (i.e. the 3:2 resonance with Jupiter). In Figure 1, the sideways “U”-shaped (or horseshoe shaped) region on the left indicates this resonance island, which contains the Hilda group of asteroids. The Hilda asteroids owe their longevity to the invariance of this resonance island. However, this island is surrounded by other orbits which give rise to interesting dynamical phenomena that have been noted in previous work. For example, comets known as quasi-Hildas, such as Oterma and Gehrels 3, appear for a time to have Hilda-type orbits until perturbed by Jupiter into a new orbit [27]. The regions of interest are given by a decomposition into almost-invariant sets, which is done in [6] with a graph partitioning algorithm (see Figure 2). The quasi-Hilda asteroid region is denoted by R and the region beyond the Mars-crosser line by Q .

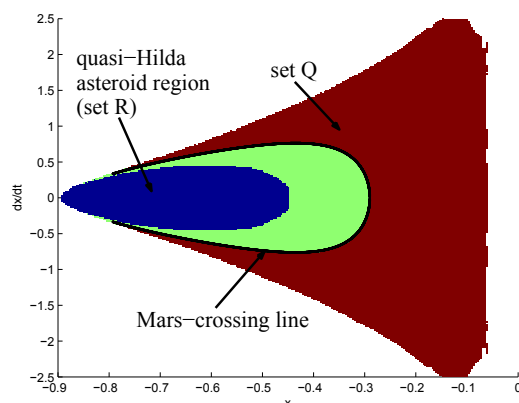


Fig. 2 (online colour at: www.gamm-mitteilungen.org) Decomposition of the Poincaré section including the quasi-Hilda region R and the region beyond the Mars-crosser line Q as used for the transport computation.

Here we are interested in computing the transfer rates between these regions by using (8), that is,

$$T_{R,Q}(k) \approx e_Q^T \mathbf{P}^k u_R. \quad (19)$$

For this computation we consider M to be the chain recurrent set within the rectangle $X = [-0.95, 0.15] \times [-2.5, 2.5]$ in the section $y = 0, \dot{y} < 0, x < 0$. M is covered by a collection of 30431 equally sized boxes and in each box we used a uniform grid of 18×18 points. In Figure 3 we show the dependence of the approximated transition probability given

by $T_{R,Q}(k)$ divided by $m(R)$, on the number of iterates k . According to this figure, the probability for a typical particle to leave the quasi-Hilda region is around 6% after 200 iterates of the map, which corresponds to a transit time between 2000 and 6000 Earth years, depending on the location of the particle within the quasi-Hilda region.

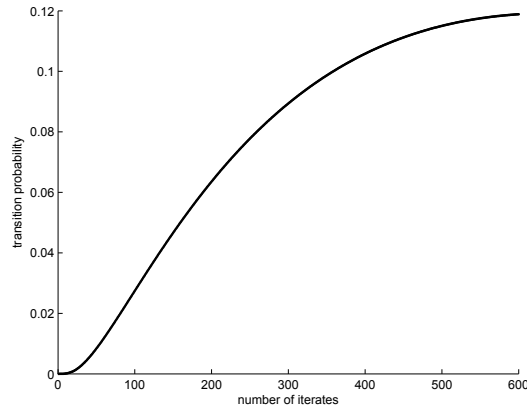


Fig. 3 Transition probability for an asteroid from the quasi-Hilda region to the Mars-crosser region as a function of the number of iterates of the return map.

5 Detection of Coherent Structures in the Southern Ocean

In this section we present two investigations of transport phenomena in the Southern Ocean based on the transfer operator approach described above. In fact, now we are interested in the approximation of almost-invariant sets as a means of detecting *coherent structures* [25, 14] in the Southern Ocean. These structures are difficult to identify as they are not revealed by the underlying Eulerian velocity fields.

In [10, 11] transfer operator techniques have been applied to identify two key coherent structures in the Southern Ocean, namely the Weddell and Ross Gyres. In a first investigation [10], the transfer operator approach identified gyre regions on the ocean surface with 10% greater coherence than standard oceanographic techniques based on sea surface height measurements. The less direct method of finite-time Lyapunov exponents was also studied in [10] and was found to perform extremely poorly.

The first study was restricted to surface ocean flow and in [11] these techniques have been extended to the full three-dimensional flow. The study [11] demonstrated that the surface gyre features reported in [10] in fact extend deep below the surface to control particle transport over large regions of the Southern Ocean. In the following we describe these investigations in more detail.

5.1 Input Data and Non-Autonomous Flow Model

In [10] only the surface of the Southern Ocean is considered. Accordingly, the domain X of the flow we are using is a subset of $\mathcal{X} = S^1 \times [-76^\circ, -36^\circ]$, with S^1 parameterized in degrees

from -180° to 180° . In the three-dimensional study in [11], X was extended to a subset of a solid annulus $\mathcal{X} = S^1 \times [-76^\circ, -36^\circ] \times [-500 \text{ m}, 0 \text{ m}]$.

In order to use our transfer operator methods described in Section 2 we have to compute trajectories of test points (see (6)). The flow of the ocean may be described by $(x, t, \tau) \mapsto \phi(x, t; \tau)$ as in Section 2, where the vector field $f : \mathbb{R} \times X \rightarrow \mathbb{R}^\ell$ in (1) is obtained from the output of the ORCA025 model [1]. This is a global ocean model, which consists of a discretization of the velocity field of the ocean and some further important ocean properties like the *sea surface height* or the *mixed layer depth*, which are explained below. The discretization is given by 3D velocity fields averaged over a month. In our computations we use data from the period January 1 to February 29, 2004.

5.2 Vertical Transport Associated with the Mixed Layer

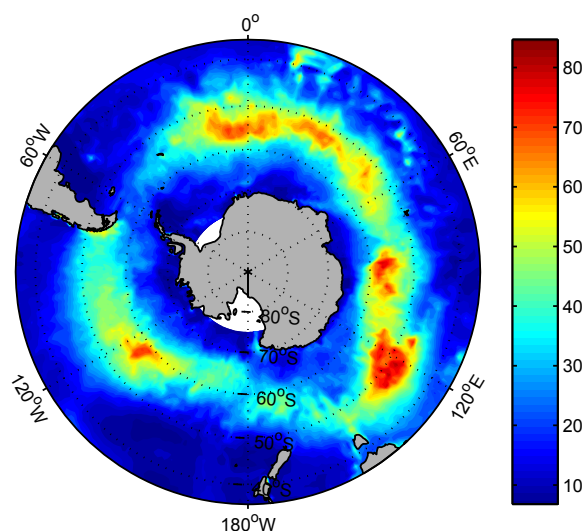


Fig. 4 (online colour at: www.gamm-mitteilungen.org) The mixed layer depth in meters on X during January 2004.

In our simulation, vertical transport of particles is dealt with in a specific way. Vertical transport associated with subduction is already included as vertical particle velocities in the ORCA025 vector field. These vertical velocities accurately represent vertical particle transport in the deep ocean. Nearer to the ocean surface, however, the mixing of particles due to wind-driven currents and the breaking of surface waves is very high. The region near the surface where this more rapid mixing occurs is called the *mixed layer* (ML). It extends from the surface down to the *mixed layer depth* (MLD). The ORCA025 model provides a monthly integrated MLD field. Within the ML, temperature and salinity are almost constant. The depth of the ML varies from day to day and from season to season.

In our three-dimensional computations we simulate mixing in the ML by assigning a new depth to each particle within the ML after one month. These new depth assignments are chosen uniformly at random within the interval between MLD and the surface.

5.3 Numerical Implementation

In both the two- and the three-dimensional case the domain \mathcal{X} is partitioned via a uniform grid of boxes $\{B_1, \dots, B_n\}$. In our computational studies we use only a subset X of \mathcal{X} where the landmass consisting of part of the continents and islands is removed.

5.3.1 Model Interpolation and Trajectory Integration

The 3D velocity fields provided by the ORCA025 model are given at a resolution of 0.25 degrees of longitude and latitude with 46 non-uniform depth layers. Velocity field values for $x \in X$ lying between grid points are affinely interpolated independently for the longitude, latitude and depth directions respectively. The velocity field $f(t, x)$ for t between grid points is produced by linear interpolation. Finally, a standard Runge-Kutta approach is used to calculate ϕ .

5.3.2 Ocean Surface Analysis

For our analysis of transport on the surface of the Southern Ocean we used the velocity field directly. We approximate the domain X by a uniform box covering $\{B_1, \dots, B_n\}$ of $n = 24534$ boxes in longitude-latitude coordinates. Each box has side lengths 0.7 degrees in longitude and 0.7 degrees in latitude. The approximation in (6) is done with $N = 400$ test points and the stepsize for the chosen Runge-Kutta approach is 1 day over a period of 60 days ($\tau = 60$). For the initial time t_0 we chose January 1, 2004.

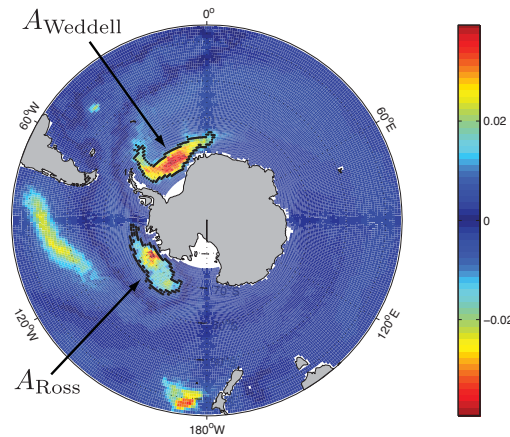


Fig. 5 (online colour at: www.gamm-mitteilungen.org) The ninth eigenvector $v^{(9)}$ calculated for a period of $\tau = 60$ days. Coherent surface structures are highlighted in the Weddell and Ross Seas. The boundary of the regions $A_{\text{Weddell}} = \{v^{(9)} > 0.01\}$ and $A_{\text{Ross}} = \{v^{(9)} < -0.01\}$, is indicated by black lines.

Following the procedure in [7] the right eigenvectors $v^{(k)}$, $k = 1, \dots, K$, corresponding to the K largest eigenvalues of $R_{t_0, \tau}$ (see (16)) are used to detect almost-invariant sets. Boxes

corresponding to large absolute values in each $v^{(k)}$ are selected. That is,

$$A = \cup_{v_i^{(k)} \geq c} B_i \text{ or } A = \cup_{v_i^{(k)} < -c} B_i \quad (20)$$

for a suitable $c \in \mathbb{R}$. In [11], the ninth eigenvector $v^{(9)}$ (corresponding to $\lambda_9 = 0.905$) identified two coherent structures in the Weddell and Ross Seas; see Figure 5. Larger coherent features were identified by the eigenvectors $v^{(k)}$, $k = 2, \dots, 8$.

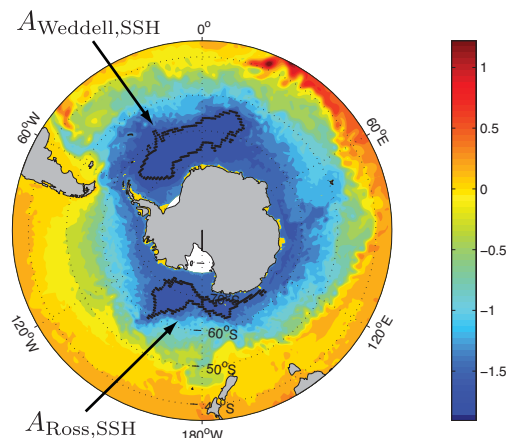


Fig. 6 (online colour at: www.gamm-mitteilungen.org) Mean SSH from ORCA025 model averaged over January 1 - February 29, 2004. The boundary of the regions $A_{\text{Weddell,SSH}} = \{\text{SSH} < -1.75 \text{ m in the Weddell Sea}\}$ and $A_{\text{Ross,SSH}} = \{\text{SSH} < -1.6 \text{ m in the Ross Sea}\}$ is indicated by black lines.

These results can be compared with those obtained from a standard technique in oceanography, the detection of gyres and eddies based on the mean sea surface height (SSH). Figure 6 shows the 60 days mean SSH over January 1 - February 29, 2004. One finds that the surface structures we located by our transfer operator approach are not precisely aligned with the locations of the Weddell and Ross Gyres as defined by the SSH computations shown in Figure 6. Indeed, there is a significant difference in the Ross Sea, confirming that our method picks up different structures to those defined simply by the SSH field of Figure 6.

We now quantify the coherence and non-dispersiveness of the structures shown in Figure 5 and 6 via equation (2). Evaluating (15) with respect to the volume of the boxes in the oceanic domain, yields $\rho_{t_0, \tau}(A_{\text{Weddell}}) = 0.91$ versus $\rho_{t_0, \tau}(A_{\text{Weddell,SSH}}) = 0.80$ and $\rho_{t_0, \tau}(A_{\text{Ross}}) = 0.85$ versus $\rho_{t_0, \tau}(A_{\text{Ross,SSH}}) = 0.75$. For example, the calculation $\rho_{t_0, \tau}(A_{\text{Weddell}}) = 0.91$ states that 91% of the surface water mass in A_{Weddell} remains (is trapped) in A_{Weddell} at time $t_0 + \tau$.

Thus the above calculations demonstrate that the regions detected by the transfer operator approach are more coherent over the 60 day period considered than those determined by sea surface height.

Remark 5.1 We remark that for comparison purposes we also employed a second technique for the detection of Lagrangian coherent structures in fluid flows, which uses finite-time

Lyapunov exponents. However it turned out, that this method is not able to identify the Weddell and Ross Gyre nearly as clearly as by our set oriented approach (see [10]).

5.3.3 Extending to Three Dimensions

For our three-dimensional analysis we extend the state space X to a subset of $\mathcal{X} = S^1 \times [-76^\circ, -36^\circ] \times [-500\text{ m}, 0\text{ m}]$. This time this domain has been approximated by a uniform three-dimensional covering by $n = 92518$ boxes. Each box has side lengths of 1.4 degrees in longitude, 1.4 degrees in latitude and 31.25 meters in depth. In this case $N = 512$ test points and a step size of 3 days has been chosen over a period of $\tau = 60$ days to calculate the matrix in (6). As in the 2D computations the starting time t_0 for the computations is January 1, 2004.

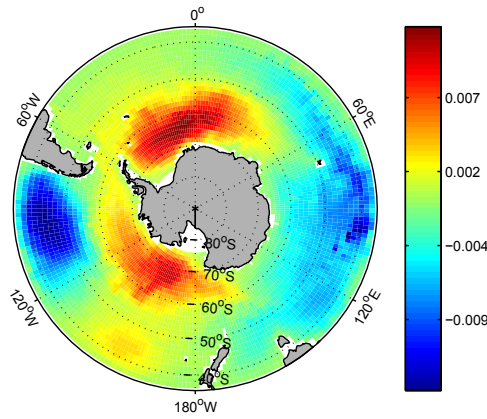


Fig. 7 (online colour at: www.gamm-mitteilungen.org) Coherent structures in the Weddell and Ross Seas are highlighted by large values of $w = v^{(4)} + v^{(6)}$. The corresponding eigenvalues are $\lambda_4 = 0.9910$ and $\lambda_6 = 0.9884$.

Among the 20 largest eigenvalues of $R_{t_0, \tau}$ (ranging from $\lambda_2 = 0.9933$ to $\lambda_{20} = 0.9796$) and the corresponding right eigenvectors, the fourth eigenvector identifies a coherent structure in the Weddell Sea and the sixth eigenvector identifies a coherent structure in the Ross Sea. In order to illustrate both structures simultaneously, a linear combination $w = v^{(4)} + v^{(6)}$ of the two eigenfunctions is considered; see Figure 7 where w is restricted to the surface. These computational results indicate that the coherent structures observed in the two-dimensional computations are indeed related to a three-dimensional phenomenon.

In order to extract the coherent structures we define sets A_c^+ and A_c^- for w as in (20) and choose c in such a way that $\min\{\rho_{t_0, \tau}(A_c^-), \rho_{t_0, \tau}(A_c^+)\}$ is maximized. This leads to three subsurface structures as part of the set A_c^+ (where $c = 0.0035$): two in the Weddell and Ross Seas respectively and another smaller one in the Southern Pacific Ocean, see Figure 8.

A coherence value of $\rho_{t_0, \tau}(A_c^+) = 0.93$ is obtained which implies that 93% of water mass is retained in A_c^+ after two months of flow. Concentrating on the Weddell and Ross regions only one finds that $\rho_{t_0, \tau}(A_c^{+, W}) = 0.93$ for the Weddell and $\rho_{t_0, \tau}(A_c^{+, R}) = 0.90$ for the Ross region.

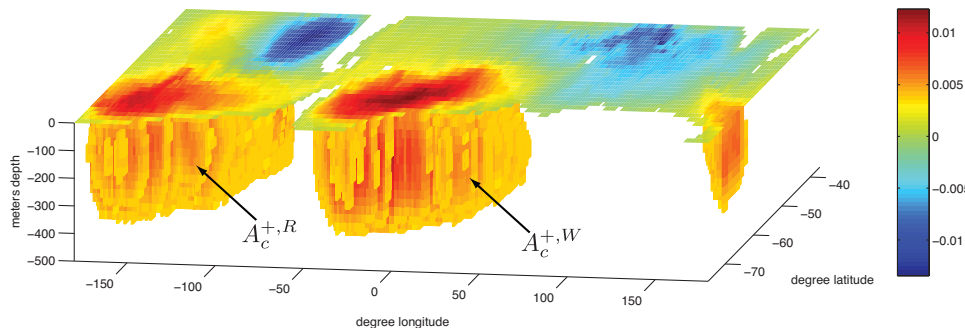


Fig. 8 (online colour at: www.gamm-mitteilungen.org) Three-dimensional coherent structures in the Weddell and Ross Seas and in the South Pacific are highlighted by large values of w . Boxes B_i with $w_i < c = 0.0035$ have been removed.

Acknowledgements This work is partly supported by the Australian Research Council (ARC) Discovery Project (0770289): “A Dynamical Systems Approach to Mapping Southern Ocean Circulation Pathways” and by the Deutsche Forschungsgemeinschaft (DFG) within the Research Training Group *Scientific Computation* (GK 693). We also thank Mirko Hessel-von Molo for fruitful discussions on the manuscript.

References

- [1] B. Barnier, G. Madec, T. Penduff, J.-M. Molines, A.-M. Treguier, J. L. Sommer, A. Beckmann, A. Biastoch, C. Boening, J. Dengg, C. Derval, E. Durand, S. Gulev, E. Remy, C. Talandier, S. Theetten, M. Maltrud, J. McClean, and B. De Cuevasm, *Impact of partial steps and momentum advection schemes in a global ocean circulation model at eddy-permitting resolution*, *Ocean Dynamics*, 5-6:543-567, 2006.
- [2] P. Brémaud, *Markov Chains: Gibbs fields, Monte Carlo simulation, and queues*, Springer, New York, 1999.
- [3] M. Dellnitz, G. Froyland, and O. Junge, *The algorithms behind GAIO – Set oriented numerical methods for dynamical systems*, *Ergodic Theory, Analysis, and Efficient Simulation of Dynamical Systems*, B. Fiedler ed., pages 145-174, Springer, 2001.
- [4] M. Dellnitz, and O. Junge, *On the approximation of complicated dynamical behavior*, *SIAM Journal on Numerical Analysis*, 36(2):491-515, 1999.
- [5] M. Dellnitz, O. Junge, W. S. Koon, F. Lekien, M.W. Lo, J. E. Marsden, K. Padberg, R. Preis, S. D. Ross, B. Thiere, *Transport in dynamical astronomy and multibody problems*, *International Journal of Bifurcation and Chaos*, 15(3):699-727, 2005.
- [6] M. Dellnitz, O. Junge, M. W. Lo, J. E. Marsden, K. Padberg, R. Preis, S. D. Ross, B. Thiere, *Transport of Mars-crossing asteroids from the quasi-Hilda region*, *Physical Review Letters*, 94(23):231102-1-4, 2005.
- [7] G. Froyland, *Statistically optimal almost-invariant sets*, *Physica D*, 200:205-219, 2005.
- [8] G. Froyland, M. Dellnitz, *Detecting and locating near-optimal almost-invariant sets and cycles*, *SIAM Journal on Scientific Computing*, 24(6):1839-1863, 2003.
- [9] G. Froyland and K. Padberg, *Almost-invariant sets and invariant manifolds – connecting probabilistic and geometric descriptions of coherent structures in flows*, *Physica D*, to appear, 2009.

- [10] G. Froyland, K. Padberg, M. England, and A.M. Treguier, *Detection of coherent oceanic structures via transfer operators*, Physical Review Letters, 98(22):224503, 2007.
- [11] G. Froyland, M. Schwalb, K. Padberg, M. Dellnitz, *A transfer operator based numerical investigation of coherent structures in three-dimensional Southern Ocean circulation*, Proceedings of the International Symposium on Nonlinear Theory and its Applications (NOLTA2008), Budapest, Hungary, 2008.
- [12] L.-L. Fu, *Pathways of eddies in the south atlantic ocean revealed from satellite altimeter observations*, Geophysical Research Letters, 33:L14610, 2006.
- [13] G. Haller, *Finding finite-time invariant manifolds in two-dimensional velocity fields*, Chaos, 10:99-108, 2000.
- [14] G. Haller, *Lagrangian coherent structures from approximate velocity data*, Physics of Fluids, A14:1851-1861, 2002.
- [15] H. Hsu, *Global analysis by cell mapping*, International Journal of Bifurcation and Chaos in Applied Sciences and Engineering, 2(4):727-771, 1992.
- [16] C.K.R.T. Jones, and S. Winkler, *Invariant manifolds and Lagrangian dynamics in the ocean and atmosphere*, Handbook of Dynamical Systems: Towards Applications, B. Fiedler ed., pages 55-92, Elsevier, 2002.
- [17] W. S. Koon, M. W. Lo, J. E. Marsden, and S. D. Ross, *Heteroclinic connections between periodic orbits and resonance transitions in celestial mechanics*, Chaos, 10(2):427-469, 2000.
- [18] W. S. Koon, M. W. Lo, J. E. Marsden, and S. D. Ross, *Resonance and capture of Jupiter comets*, Celestial Mechanics and Dynamical Astronomy, 81(1-2):27-38, 2001.
- [19] W. S. Koon, M. W. Lo, J. E. Marsden, and S. D. Ross, *Low energy transfer of the Moon*, Celestial Mechanics and Dynamical Astronomy, 81(1-2):63-73, 2001.
- [20] W. S. Koon, M. W. Lo, J. E. Marsden, and S. D. Ross, *Constructing a low energy transfer between Jovian moons*, Contemporary Mathematics, 292:129-145, 2002.
- [21] E. Kreuzer, *Numerische Untersuchung nichtlinearer dynamischer Systeme*, Springer-Verlag, New York, 1987.
- [22] F. Lekien, C. Coulliette, and J. E. Marsden, *Lagrangian structures in very high frequency radar data and optimal pollution timing*, American Institute of Physics: 7th Experimental Chaos Conference, CP676:162-168, 2003.
- [23] K. Padberg, *Numerical analysis of transport in dynamical systems*, Ph.D. thesis, University of Paderborn, 2005.
- [24] J. Peng, J. O. Dabiri, *Transport of inertial particles by Lagrangian coherent structures: application to predator-prey interactions in jellyfish feeding*, Journal of Fluid Mechanics, to appear, 2009.
- [25] S. C. Shadden, F. Lekien, and J. E. Marsden, *Definition and properties of Lagrangian coherent structures from finite-time Lyapunov exponents in two-dimensional aperiodic flows*, Physica D, 221(3-4):271-304, 2005.
- [26] S. C. Shadden and C. A. Taylor, *Characterization of coherent structures in the cardiovascular system*, Annals of Biomedical Engineering, 36(7):1152-1162, 2008.
- [27] C. E. Spratt, *The Hilda group of minor planets*, Journal of the Royal Astronomical Society of Canada, 83:393-404, 1989.
- [28] V. Szebehely, *Theory of orbits*, Academic Press, New York-London, 1967.
- [29] S. Ulam, *A collection of mathematical problems*, Interscience Publishers, New York, 1960.
- [30] S. Wiggins, *The dynamical systems approach to Lagrangian transport in oceanic flows*, Annual Review of Fluid Mechanics, 37:295-328, 2005.